HEAVY ION FUSION SCIENCE VIRTUAL NATIONAL LABORATORY 3rd QUARTER 2010 MILESTONE REPORT

Assess the key physics that underpins high-hydro coupling-efficiency in NDCX-II experiments and high-gain heavy ion direct drive target designs using proven hydro codes like HYDRA.

J. J. Barnard, M. J. Hay, B. G. Logan, S. F. Ng, L. J. Perkins, S. Veitzer, S. S. Yu

1. Executive Summary

Milestone's Potential Impact —The simulations provided in this milestone have solidified the theoretical underpinning of direct drive targets and also the ability to design experiments on NDCX II that will enhance our understanding of ion-beam hydrodynamic coupling, and thus be relevant to IFE. For the case of the IFE targets, we have studied hydro and implosion efficiency using HYDRA in 1D, a starting point towards the goal of polar direct drive in geometry compatible with liquid wall chambers.

Recent analysis of direct drive fusion energy targets using heavy ion beams has found high coupling efficiency of ion beam energy into implosion energy. However, to obtain optimal coupling, the ion energy must increase during the pulse in order to penetrate the outflowing ablated material, and deposit the energy close enough to the fuel so that the fuel achieves sufficient implosion velocity. We have computationally explored 1D (radial) time dependent models of ion driven direct drive capsule implosions using the Arbitrary Lagrangian-Eulerian (ALE) code HYDRA, to help validate the theoretical analysis done so far, particularly exploring the effects of varying the ion energy and ion current over the course of the pulse. On NDCX II, experiments have been proposed to explore issues of ion penetration of the outflowing plasma over the course of the ion pulse. One possibility is to create a first pulse of ions that heats a planar target, and produces an outflow of material. A second pulse, ~10 ns after the first, of higher ion energy (and hence larger projected range) will interact with this outflow before reaching and further heating the target. We have investigated whether the change in range can be tailored to match the evolution of the ablation front. We have carried out simulations using the one-dimensional hydrodynamic code DISH and HYDRA to set parameters for this class of experiments. DISH was upgraded with an ion deposition algorithm, and we have carried out 1D (planar) simulations. HYDRA was also used for 1D (planar) and 2D (r,z) simulations of potential experiments. We have also explored whether similar physics could be studied using an energy ramp (i.e., a velocity tilt) rather than two separate pulses. We have shown that an optimum occurs in the macropulse duration (with fixed velocity tilt) that maximizes the shock strength.

In the area of IFE target design we have continued to explore direct drive targets composed of deuterium-tritium fuel and ablator layers. We have extended our

previous target designs at 0.44 MJ drive energy, gain 50, (50 MeV foot, 500 MeV main pulse, Rb ion, (which requires a large number of beams due to a high beam space charge constraint) to a power plant scale 3.7 MJ drive energy, gain ~150 (220 MeV foot, 2.2 GeV main pulse, Hg ion) that eases requirements on the accelerator. We have studied the effects of two important design choices on ICF target performance. We have shown that increasing the number of foot pulses may reduce the target's in-flight adiabat and consequently improve its compressibility and fusion yield. As in the case of laser drive, the first three shocks are the most important to the target's performance, with additional shocks contributing only marginally to compression and burn. We have also demonstrated that ion range lengthening during the main pulse can further reduce the target adiabat and improve the efficiency with which beam energy is coupled into the target. (Ion range lengthening using two different kinetic energies for the foot and main pulse has previously proven effective in the design of high gain targets).

2. Results: Simulations of hydrodynamic coupling experiments on NDCX-II and direct-drive IFE targets

Table of Contents: We divide this report into two sections, each describing an advance in understanding. The two sections are: 2-I. Simulations of hydrodynamic coupling on NDCX-II; and 2-II. Simulations of direct-drive IFE targets

2-I. Simulations of hydrodynamic coupling on NDCX-II (S.F. Ng, S.A. Veitzer, J.J. Barnard, and S.S. Yu).

2-I-1. Introduction In inertial fusion targets, a hollow spherical shell of deuterium-tritium (DT) fuel is imploded by the pressure of a surrounding ablator shell, which is rapidly heated either directly by laser irradiation, indirectly by X-rays inside a hohlraum, or directly by particle-beam deposition. Intense heavy ion beams have some advantages as drivers for Inertial Fusion Energy (IFE) [1, 2, 3], such as their high efficiency, intrinsically high repetition rate, and their attractive final focus and chamber solutions. Direct deposition of ion beam energy to potential IFE targets is a well-studied process and ion beam heating, in contrast to laser induced heating, is much more uniform across macroscopic targets. To achieve an efficient implosion of an IFE target, a high coupling efficiency is needed. Coupling efficiency is the ratio of the total material kinetic energy propagating inwards (in the spherical target) to the total deposited ion beam energy. A higher coupling efficiency allows the driver energy to be reduced and so reduces the cost of the driver. However, as with laser drivers, using a heavy-ion direct-drive target has to overcome decoupling, whereby ablated material created early in the ion pulse absorbs energy from subsequent parts of the beam, decreasing the effectiveness of the energy deposition. This can reduce the peak ablation pressure at the inner surface of the IFE target, and so reduces the coupling efficiency. There are several potential methods for reducing decoupling of the beam discussed in recent literature [4]. The most direct way is to increase the beam energy during the later state of the drive so that the beam can penetrate the outgoing ablation plasma exhaust and still deposit most of its energy close to the region of peak ablation pressure front during the implosion. An approximation for this is to use two distinct beams, with the second beam having a higher energy than the first. One goal of simulation is to determine what combination of beam energies will maximize the efficiency of energy deposition. In this report, we simulate dual pulses of ion beams impacting possible targets relevant to a near-term experimental facility at LBNL (the Neutralized Drift Compression Experiment-II, NDCX-II) [5], which is for the studies of warm dense matter and inertial fusion energy. NDCX-II is planned to have a Li^+ ion beam with energy of 1-3 MeV and 0.02 -0.03 μC charge in a sub ns pulse. For the purposes of this paper we adopt a standard design with 2.8 MeV, 0.03 μC, 1 ns Li+ ion beam, with 30 J/cm^2 central fluence, although various ion energies are used as examples. In a slab geometry target, an intense ion beam propagating from a single direction heats the target and hydrodynamic simulations are carried out for various ion energy time profiles. The cases of using two separate pulses with different ion energies and one single pulse with ramping ion energy are simulated and an increase in coupling efficiency is observed. Both solid materials and

porous materials are examined.

2-I-2. 1-D Slab Hydrodynamic Simulation In solid density metallic targets beam ions have a short range (< 10 μm) for the parameters considered here and a relatively large beam radius (~ 0.5 mm) in comparison with the ablative target thickness (~ 30 μm). We first treat this case using a 1-Dimensional hydrodynamic Lagrangian code with slab (Cartesian) geometry called DISH (originally standing for a deeply simplified hydrodynamic code for applications to warm dense matter) [6]. Hydrodynamic evolution of the targets is coupled with deposition of ion beam energy.

We model the ion energy deposition, or stopping power, with a modified Bethe-Bloch formulation [7, 8].

$$-\frac{dE}{dx} = \left[\frac{4\pi e^2}{m_e c^2}\right]\left[\frac{N_0 \rho_T}{A_T}\right]\left[\frac{Z_{eff}^2}{\beta^2}\right]\left\{(Z_T - \bar{Z})(\text{Log}\,\Lambda_B + R) + \bar{Z}G(\beta/\beta_e)\left(\text{Log}\,\Lambda_F + R/2\right)\right\} \quad (1)$$

Here ρ_T, A_T, Z_T, and $\bar{Z}$ are the target density, target atomic weight, target atomic number and target ionization state, respectively. The stopping logarithms Λ_B and Λ_F are given by:

$$\Lambda_B = 2m_e c^2 \beta^2 / \bar{I} \quad (2)$$

$$\Lambda_F = m_e c^2 \beta^2 / (\hbar\omega_p) \quad (3)$$

and the Chandrasekhar function *G(x)* is given by

$$G(x) = \text{erf}(x) - x\, d[\text{erf}(x)]/dx \quad (4)$$

$G(x) \approx 1$ for $x >> 1$, where erf(x) is the error function of x; $\bar{I}$ is the average ionization potential, given approximately by Bloch's rule as $\bar{I} \approx 0.01 Z_T$ keV; $\omega_p \equiv \sqrt{4\pi e^2 n_e / m_e} = 56416\sqrt{n_e}\ \text{s}^{-1}$ is the plasma frequency, $n_e = \bar{Z} N_0 \rho_T / A_T$ and $\hbar\omega_p \approx 3.7 \times 10^{-14}\sqrt{n_e}$ keV, where n_e is measured in cm^{-3}. Also, $\beta = v/c$ is the ion beam velocity in units of the speed of light c, and the Lorentz factor of the ion beam γ, is given by $\gamma = 1/\sqrt{1-\beta^2} = 1 + E/Mc^2$, where E is the kinetic energy of the ion beam, Mc^2 is the rest energy of an ion with atomic mass A_{IonBeam}. The electron rest energy is $m_e c^2$. R is a relativistic correction, given by $R = 2\ (\log \gamma) - \beta^2$. Also, the effective charge state of the ion was given by the Betz formula:

$$Z_{eff} = Z_{IonBeam}\left[1 - \exp(-137\beta_{eff} / Z_{IonBeam}^{0.69})\right] \quad (5)$$

where $\beta_{eff}^2 = \beta^2 + \beta_e^2$ and with $\gamma_e = 1/\sqrt{1-\beta_e^2} = 1 + kT_e / m_e c^2$.

The ion-stopping model described above includes terms for both bound and free electrons and is sufficiently accurate for purposes considered here. We do not

consider the contribution of Coulomb scattering off nuclei to ion stopping in this study. For the cases in this paper, the target is not hot enough to be fully or nearly fully ionized and the dominant mechanism for ion energy loss is by ion collisions with bound target electrons. In this paper, we model Li^+ ion beams incident on a variety of targets, such as lithium hydride and underdense aluminum foam. In the simulations, we use the quotidian equation of state (QEOS) [9] as the equation of state of the material. And the QEOS data used in the DISH code are calculated by the MPQeos code [10]. In QEOS, the electronic properties are obtained from a modified Thomas-Fermi statistical model, while the ion thermal motion is described by a multiphase equation of state combining Debye, Gruneisen, Lindemann, and uid-scaling laws. QEOS can give smooth predictions for ionization state, pressure, energy, entropy and Helmholtz free energy for use in hydrodynamic simulations.

2-I-3. Simulation Results

2-I-3.1 1D simulations of Lithium Hydride target: We simulate the beam-target interaction using 35 μm thick lithium hydride (LiH) as target. Lithium hydride is a low density solid (about 0.82 g/cm^3) at room temperature so it can be compressed by a shock wave relatively easy compared to higher density solids. As a result, the material kinetic energy inside the target can be higher and so a higher coupling efficiency may be obtained. In the dual pulse simulations, the first ion pulse impacts the target with relatively low energy (1 MeV) and with duration 1 ns. The ion range is about 10 μm in LiH, and so the first part of the target is heated to nearly 0.6 eV. The heated part will generate a shock wave propagating in the direction of the beam (longitudinal direction) that will compress the target material during propagation. After the first pulse ends at t = 1 ns, the shock front has moved to a certain position inside the target and 1 ns later (at t = 2 ns), a second pulse impacts the target so as to enhance the kinetic energy of the material of the shock. If the second pulse has the same energy as the first one, the ion energy will be deposited in a region well behind the shock front. So the propagation of the shock will not be affected, since the shock wave is propagating faster than the sound speed. We then adjust the ion energy of the second pulse to deposit the bulk of its energy just behind the shock front. Then the kinetic energy of the shock will be maximized.

Fig. 1 shows the velocity profiles of the target material at different simulation times for different dual pulse beam parameters. In Figure 1c, we use a first pulse with energy of 1 MeV impacting the target at from t = 0 to t = 1 ns. And the second pulse with energy of 1 MeV is turned on at t = 2 ns. It is noticed that after the shock wave passes through the whole target, at time between t = 3 to 4 ns, the velocity of the material as the shock propagates into vacuum are much higher than when it propagates in the bulk, as it propagates at lower density and higher velocity, outside the bulk conserving momentum.

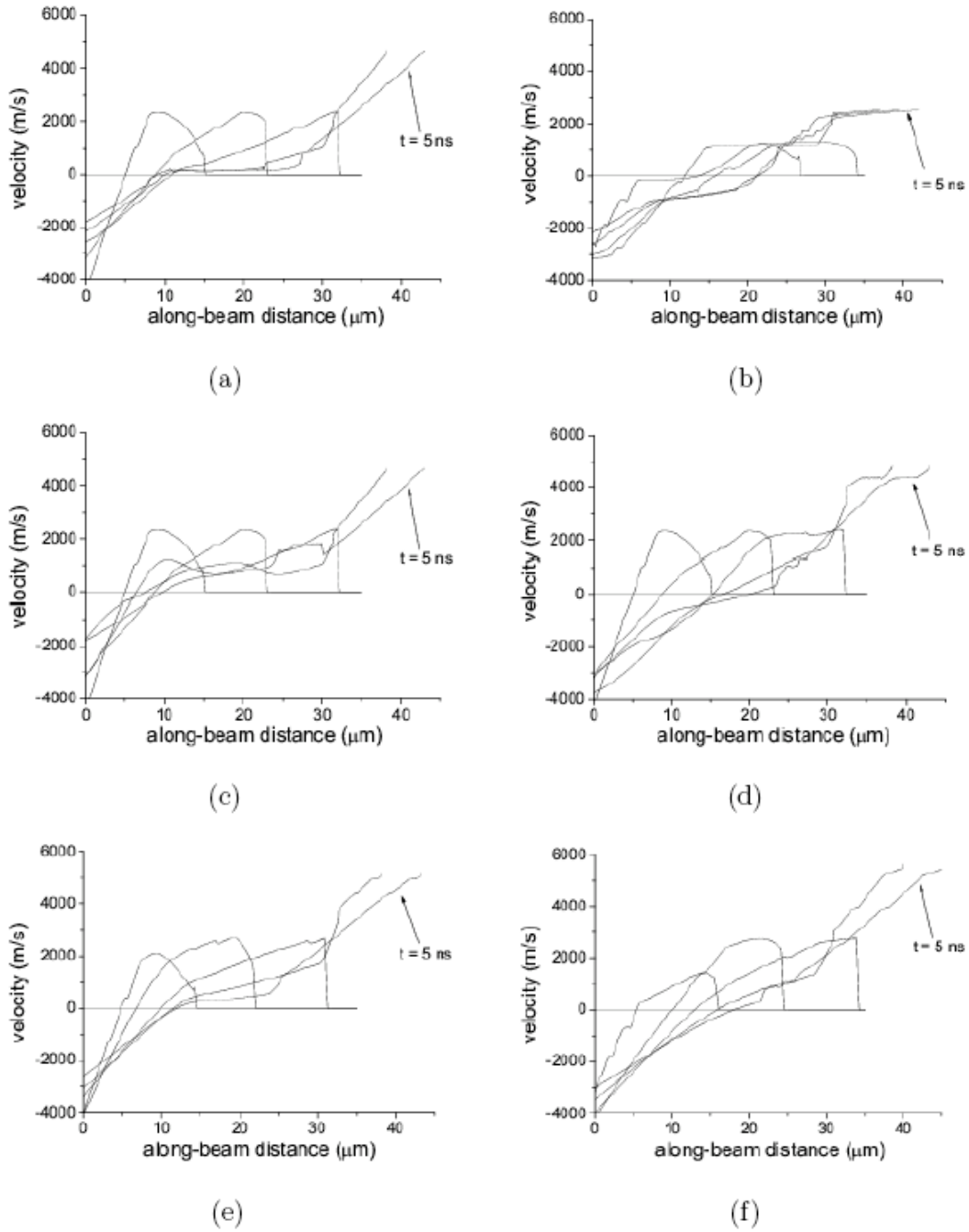

Figure 1. Velocity profiles for lithium hydride target at t = 0, 1, 2, 3, 4, and 5 ns for the cases of (a) single pulse with energy of 1 MeV, (b) single pulse with energy of 2.3 MeV, (c) double pulses both with energy of 1 MeV, (d) first pulse of 1 MeV and second pulse of 2.3 MeV, (e) single long pulse with constant energy of 1 MeV, and (f) single long pulse with linearly ramping energy from 1 to 2.3 MeV.

We find that the velocity profiles near the end of the target (at longitudinal distance of about 30 to 40 μm) are very close to that for the case of only the first pulse (Figure 1a). This means that the second pulse of the same energy as the first pulse does not enhance the kinetic energy of the material and so the coupling efficiency. In

comparison, Figure 1d shows the case of second pulse with energy of 2.3 MeV so that the ion of the second pulse will stop just behind the shock front at t = 2 ns. It is noticed that before t = 2 ns, the profiles of the cases in Figure 1a, c and d are the same. In Figure 1d, at around the end of the target, more material is moving with high velocity (when it is compared to Figure 1c). It means that the more ion beam energy can change to be the kinetic energy of the material and so the coupling efficiency will be enhanced. Figure 1b shows the case of only one pulse with energy of 2.3 MeV turned on at t = 0 to 1 ns with the same beam power (beam current density times ion energy divided by ion charge, in unit of energy per unit area per unit time) as the case shown in Figure 1a. Because a higher ion energy beam has a larger ion range, the energy deposition will be dispersed to a larger region and so the target will just be heated to a lower temperature (0.3 eV). So the material will have a lower velocity when it is leaving the target. Within the time that the ion beam is turned on, i.e. from t = 0 to 1 ns and from t = 2 to 3 ns in Figure 1c and d, the shock wave is still moving with a relatively high speed. So at the later part of each beam, the ion energy is not deposited so as to affect the shock wave kinetic energy. So to maintain the maximum energy deposition right behind the shock front, it may be necessary to ramp the ion energy in a single pulse, i.e. to use one single ion beam with ramping ion energy so that the ions are always stopping at the shock front. Figure 1e and f show the velocity profiles of the material at different time for 2 cases. For both cases, we have one single pulse of duration 2 ns with different ion energy profiles. In Figure 1f, we choose to ramp the beam energy linearly from 1 to 2.3 MeV, such that the ion beam always ends at a position close to the shock front. In Figure 1e, we use a beam of constant ion energy of 1 MeV for comparison. The figures show that if we use a beam with ramped ion energy, the velocity, and so the coupling efficiency will be enhanced. To have a more quantitative idea of how the coupling efficiency can be improved by the above methods, we may calculate the coupling efficiencies as a function of time for all 6 cases, which is shown in Fig. 2. For all the cases, the beam powers are the same (30 J/cm^2/ns). So for cases a and b, the total ion energy deposited in the target is 30 J/cm^2 and for all other cases, it is 60 J/cm^2. Fig. 2 shows that using a ramped ion energy in a single long pulse leads to the maximum coupling efficiency (~ 15%). This is because using this method, the ion energy deposition follows closely behind the imploding ablation front and so this method maximizes the kinetic energy of the material that has positive velocity.

2-I-3.2 1D Simulation of underdense Aluminum foam: We have also modeled Li^+ impacting 50% solid density aluminum foam using both DISH and HYDRA. We examine four cases in the 1D simulations. First, we simulated two 1 ns pulses, each with 1.0 MeV energy. Second, we simulated two 1 ns pulses, where the first pulse has 1.0 MeV, and the second is 1.3 MeV. Third, we simulated a single 2 ns pulse with constant energy of 1.0 MeV, and finally, we examined a single 2 ns pulse with linearly ramped energy from 1.0 to 1.3 MeV. The coupling efficiencies for these four cases are shown in Figure (3). The beam power and the total energy depositions to the target for all cases are 30 J/cm^2/ns and 60 J/cm^2. Similar to the case for lithium hydride, we find that using a single ramped ion energy in a long pulse achieves the maximum coupling efficiency, although the spread in efficiencies is quite small

between the different cases.

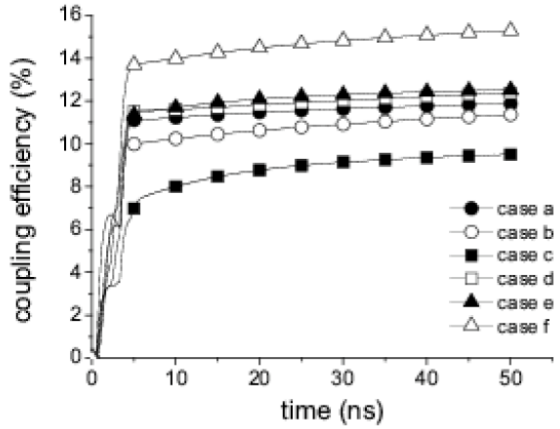

Figure 2. Coupling efficiency as a function of time for the cases of (a) single pulse with energy of 1 MeV, (b) single pulse with energy of 2.3 MeV, (c) double pulses both with energy of 1 MeV, (d) first pulse of 1 MeV and second pulse of 2.3 MeV, (e) single long pulse with constant energy of 1 MeV, and (f) single long pulse with linearly ramping energy from 1 to 2.3 MeV.

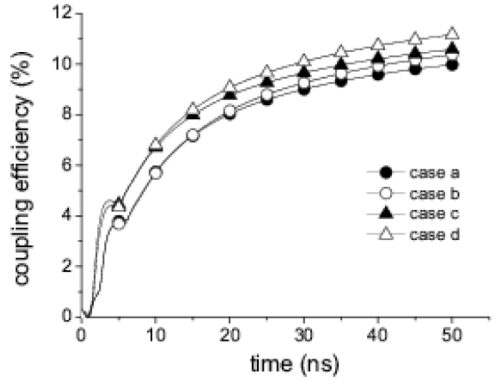

Figure 3. Coupling efficiency as a function of time for the cases of (a) double pulses both with energy of 1 MeV, (b) first pulse of 1 MeV and second pulse of 1.3 MeV, (c) single long pulse with constant energy of 1 MeV, and (f) single long pulse with linearly ramped energy from 1 to 1.3 MeV.

2-I-3.3 3D Simulation of Underdense Aluminum Foam We have also done simulations of dual pulses of NDCX-like beams incident on underdense targets using HYDRA in various pulse energies. The HYDRA simulation package is a 3D multiphysics radiation hydrodynamics code, eg. [11]. It contains implementations of state-of-the-art physics algorithms covering shocks, opacities, radiation transport, and electron and ion conduction. As with the DISH simulations, we use a modified Bethe-Bloch stopping power formulation for ion deposition. HYDRA offers a number of different Equations of State. In these simulations we used a QEOS model, in which a Cowan-type model is used for ions and electron EOS is computed using scaled Thomas- Fermi tables.

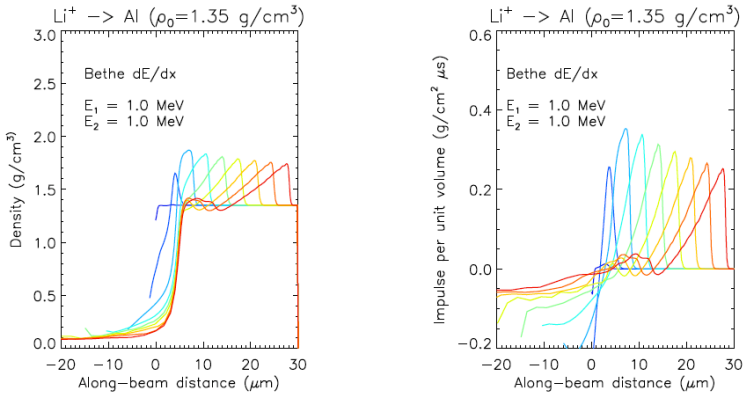

Figure 4. Target density and specific impulse for two pulses, both with 1.0 MeV energy.

In our simulations, we simulated a number of dual pulse beam/target combinations using HYDRA. All of the simulations were comprised of two beams of duration 1 ns (lab frame), separated by 1 ns. The targets were 30 μm thick in the beam direction, initially uniform density. We considered dual pulses incident on a number of different targets, including solid density argon and aluminum, and underdense aluminum foam targets, which we describe here. Our results are consistent with the 1D simulations described above. For simulations with two beam pulses of equal energy, there is no enhancement in the target density or longitudinal velocity, because the second pulse experiences target material that is blown off the front face by the first beam. The second beam loses some amount of energy in the low-density material, and the shock from the second beam can not catch up to that of the first beam. So in the case of equal energies, the two pulses are decoupled in the target. This can be seen in figure (4), which shows the density and impulse per unit volume (target material density times velocity) for two 1.0 MeV pulses incident on 50% solid density aluminum foam. In cases where the second pulse had greater energy than the first, we observed enhancements in the target density and target material velocity. For instance, figure (5) compares the target density profiles at different times for a single 6.0 MeV beam of lithium and a dual pulse simulation with the first beam having energy of 1.0 MeV, 7 followed by a 6.0 MeV pulse. As can be seen in the figure, there is an increase in peak density of nearly 15% over the single beam case. The projected range of 1.0 MeV Lithium in this target is approximately 5 μm, while for 6.0 MeV lithium the range is about 25 μm. The conclusion is that although the first beam deposits all of its energy near the front surface of the target, it is able to create a density shock wave that propagates into the target and is enhanced by the second beam. Additionally, the steepness of the density shock wave is enhanced by using two beam pulses instead of a single pulse. Similarly, a 100% increase in the longitudinal velocity, as well as an increase in the shock steepness is observed in this case. This leads to an overall doubling of the impulse per unit volume at the back end of the target when dual pulses are used, as is demonstrated in figure (6).

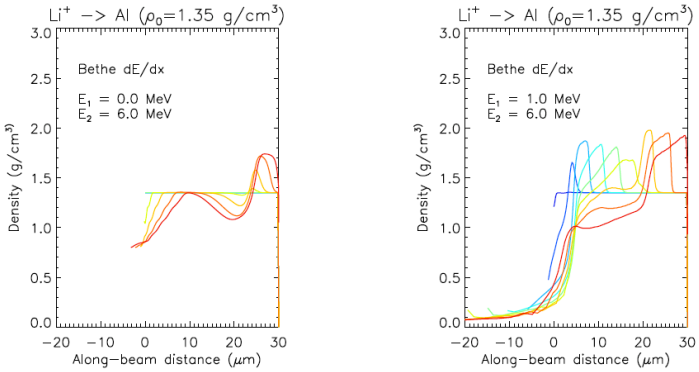

Figure 5. Density profile evolution for lithium in 50% solid density aluminum targets.

It is interesting to note in the figures above that the 1.0 MeV beam generally creates a stronger shock wave than 6.0 MeV beams. This is because a 1.0 MeV beam, being below the Bragg peak energy of about 1.9 MeV, deposits all of its energy in a very localized region of the target. 6.0 MeV beams however have a very spread out region of deposition, giving rise to a much larger width for the propagating shock. To understand this effect, we also considered a number of other beam energy combinations. For example, figure (7) shows dual pulse results for two lithium beams in 50% solid density aluminum targets with energies of 500 keV and 2.8 MeV. The ratios of beam energies are approximately the same as the case described above. However, the overall beam energy is significantly less than in that case. Here, the projected ranges are approximately 3μm for the 500 keV beam, and only about 11μm for the 2.8 MeV beam. In this case, it is clear that the shock from the second beam does not have sufficient velocity to catch up with the first shock over the depth of the target (30 μm). However, the peak density reaches about 1.7g/cm^3, which is the same as for a single 6.0 MeV beam. The peak velocity is about 1.5 cm/μs, which is 50% larger than for the 6.0 MeV single beam case. The implication is that lower energy beams may be useful in producing shocks at the back of HIF targets for compression, and that the beam energies may be tuned such that the peak shock is

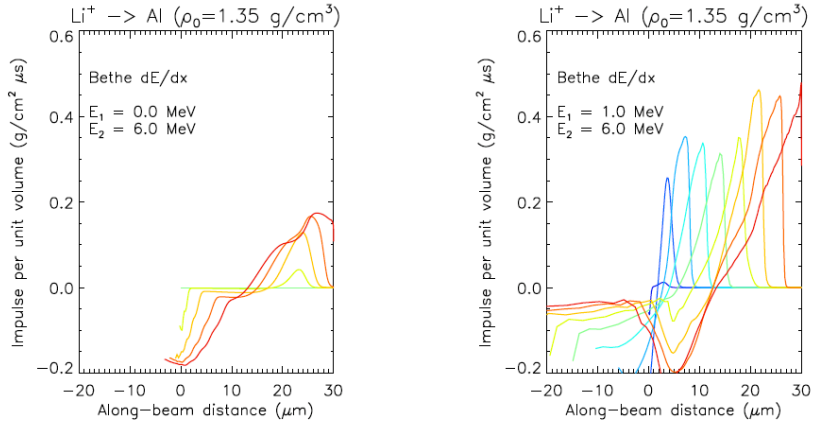

Figure 6. Impulse profile evolution for lithium in 50% solid density aluminum targets. achieved at the back of the target.

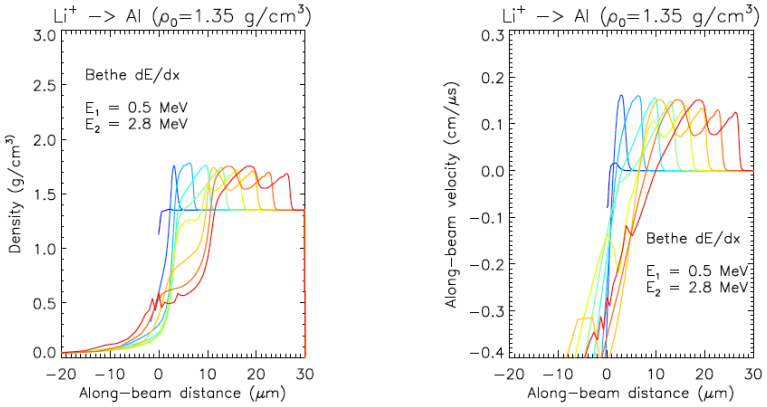

Figure 7. Density and longitudinal velocity profiles for low-energy dual pulse beams in 50% solid density aluminum targets. Significant enhancements in the density and velocity are achieved, and good shock steepness is also seen.

2-I-3.4. Optimization of the ramp rate: In this section, we give another example of a possible target that could be tested on NDCX-II. As has been discussed in section 2-I-3.3, ramping the ion beam over time is an efficient way to match the ion penetration depth to the propagating shock. In this section, we use the HYDRA code, and approximate a continuous ramp by assuming the pulse is the sum of n individual pulses, each with a parabolic time profile with 1 ns full width, but with the beginning of each pulse separated in time by an amount Δt. (The full width of the pulse is then $[n\text{-}1]\Delta t$ + 1 ns). Typically, we chose n=5 for our simulations. See figure 8.

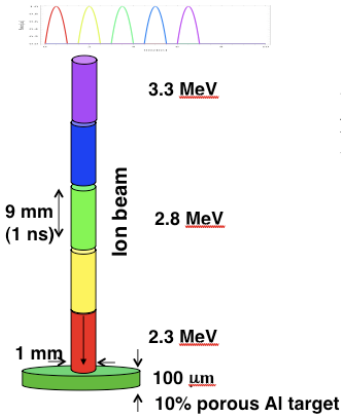

Figure 8. Schematic of simulation of a continuously varying ion energy, by approximating the beam as 5 pulses with linearly increasing energy, impinging upon a 100 μ thick 10% porous Aluminum target. Each pulse is parabolic in time as indicated in upper part of figure.

We may first estimate how rapidly we need to slew the energy of the ion beam. Near the Bragg peak, the ion energy loss rate dE/dX does not vary rapidly, and the ion range Δz is proportional to E/(dE/dX) where E is the ion energy. The ion range is thus approximately proportional to the energy (for energies near the Bragg peak). For solid aluminum we can write this approximately as $\Delta z \approx 2\mu\left(E/1\ \text{MeV}\right)$. If we assume that

the shock wave (for weak shocks) propagates at the sound speed then the slew rate must approximately satisfy:

$$\frac{dE}{dt} = E\frac{c_s}{\Delta z} \cong \begin{cases} 1.50\ \dfrac{\text{MeV}}{\text{ns}} & \text{(solid Al)} \\ 0.05\ \dfrac{\text{MeV}}{\text{ns}} & \text{(10\% Al foam)} \end{cases}$$

For aluminum foam, we assume c_s is lower (~1 μ/ns) relative to solid (~3 μ/ns), and the range is inversely proportional to the density. Preliminary WARP simulations indicate that slew rates of order 0.1 MeV/ns are easily achievable upstream of the longitudinal focus on NDCX-II, so that experiments in aluminum foam would be possible.

Fig. 9 illustrates snapshots of HYDRA simulations of the longitudinal fluid velocity and the density for an energy "slewing" Lithium ion pulse propagation in 10% Aluminum foam, with a mean ion energy of 2.8 MeV, an energy tilt of ±18%. The total fluence in all cases corresponded to 30 J/cm^2. As can be seen the density compresses to near solid density and a well formed shock is formed. Figs. 10 and 11 show an overlay of two snapshots (separated by 2 ns) of longitudinal velocity and density from which we may calculate the shock velocity. For the 1 ns macropulse (at the longitudinal focus) the shock velocity was 1.0 μ/ns, the fluid velocity behind the shock was 0.9 μ/ns, and the fluid density jumped from 0.27 g/cm^3 to 2.2 g/cm^3. For the 7 ns macropulse the shock velocity was 1.8 μ/ns, the fluid velocity behind the shock was 1.6 μ/ns, and the fluid density also jumped from 0.27 g/cm^3 to 2.2 g/cm^3. The shock strength maximized at a 7 ns macropulse (see fig. 10), corresponding to a slew rate of approximately 1 MeV in 7 ns, or 0.14 MeV/ns, somewhat higher than higher than our estimate above, largely because the shock speed is 1.8 μ/ns, higher than our estimate of 1 μ/ns.

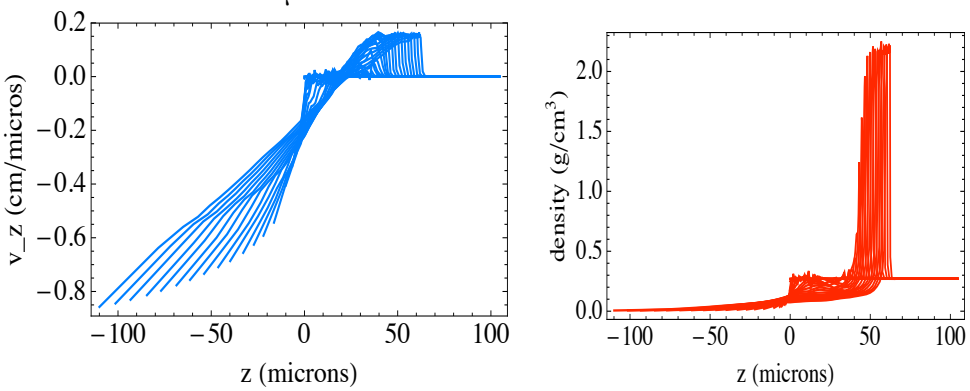

Figure 9. Overlay of 14 snapshots from HYDRA of longitudinal fluid velocity (left) and mass density (right) at radial center of target described in fig. 8. The total pulse duration in this example was 6 ns.

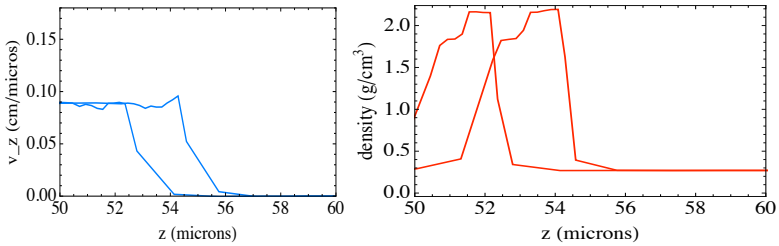

Figure 10. Overlay of 2 snapshots of longitudinal fluid velocity (left) and mass density (right) at radial center of target described in fig. 8. The total pulse duration in this example was 1 ns.

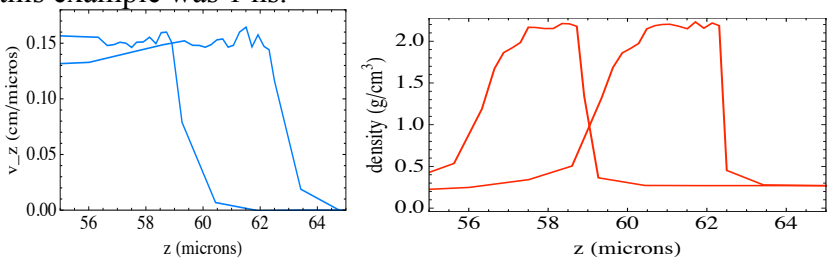

Figure 11. Overlay of 2 snapshots of longitudinal fluid velocity (left) and mass density (right) at radial center of target described in fig. 8. The total pulse duration in this example was 6 ns.

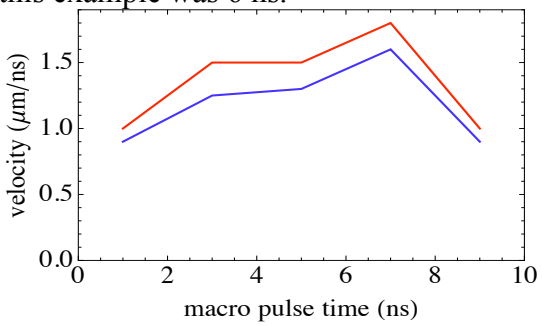

Figure 12. Fluid velocity (lower curve in blue) and shock velocity (upper curve in red) demonstrating an optimum coupling at a macro pulse time of 7 ns. (The longitudinal focus (minimum pulse time occurs at 1 ns.)

2-I-4. Conclusion In inertial confinement fusion energy experiments using intense heavy ion beams, a high coupling efficiency leads to more efficient implosion of the target. This section has investigated ways to enhance coupling efficiency in an inertial fusion target. The basic idea to enhance the coupling efficiency is to deposit ion energy in the material propagating in the same direction as the ion beam, i.e. to the position just behind the shock front. We can generate a shock wave propagating inside the target by an ion beam first and then heat the target with another beam (or the later part of the same beam) with higher ion energy so that the ions will stop at a position close to the shock front. The energy deposition near the shock front can increase the shock strength and the flow kinetic energy of the material propagating in the direction of the beam and so results in a high coupling efficiency. Ramping the ion beam energy may be a good and easy method to achieve this. If we ramp the ion energy of a single ion beam pulse, the ion range of the same ion pulse will have an increasing ion range. So after the head of the pulse generates a shock and the shock propagates, the tail of the pulse can still hit the shock front and deposit energy close

to the shocked material. Simulations show that using this method of ramping energy can have the largest coupling efficiency when compared to other ion energy time profiles tested. The maximum coupling efficiency can go up to about 11 to 15 % for these parameters.

Acknowledgments We thank A. Friedman, P. T. Leung, B. G. Logan and R. M. More for discussions. We also thank R. M. More for providing the DISH code for hydrodynamic simulations, and A. J. Kemp and J. Meyer-ter-Vehn for providing MPQeos code for calculating QEOS data.

2-I-5. References

[1] F. M. Bieniosek et al., Nucl. Instr. and Meth. A 577, 284 (2007).
[2] J. J. Barnard et al., Nucl. Instr. and Meth. A 577, 275 (2007).
[3] L. R. Grisham, Phys. Plasmas 11, 5727 (2004).
[4] B. G. Logan, L. J. Perkins, and J. J. Barnard, Phys. Plasmas 15, 072701 (2008).
[5] W. L. Waldron et al., Plans for warm dense matter experiments and IFE target experiments on NDCX-II, Conference paper: TOFE 2008 (2008).
[6] R. M. More, DISH code and DISH user manual (2007).
[7] T. Kaiser, G. Kerbel, and M. Prasad, unpublished LLNL presentation Implementing ion beams in Kull and Hydra (1999)
[8] S. Atzeni, and J. Meyer-Ter-Vehn, The Physics of Inertial Fusion: Beam Plasma Interaction, Hydrodynamics, Hot Dense Matter (Oxford University Press, 2004).
[9] R. M. More, K. H. Warren, D. A. Young, and G. B. Zimmerman, Phys. Fluids 31, 3059 (1988).
[10] A. Kemp and J. Meyer-ter Vehn, Nucl. Instr. and Meth. A 415, 674 (1998).
[11] M. M. Marinak and O. S. Jones and G. D. Kerbel and N. Gentile and S. M. Pollaine and S. W. Haan, "Integrated 3D modeling of NIF ignition targets", 44th Annual Meeting of the Division of Plasma Physics, 2002.

2-II. Simulation of IFE Targets (M. Hay, J. Barnard, J. Perkins)

II-2-1. Introduction: In this section we use 1D HYDRA simulations to build upon our recent work [1] that presented 1D direct drive target designs with low pulse energy and high gain. High gain was obtained partly as a result of the high target coupling efficiency enabled by using ion beams as drivers. For this report, we scale the target from ref. [1] to higher pulse energy (more representative of a power plant in scale) with a higher ion energy (that eases requirements on the ion accelerator). In section II-2-2, we describe the scaling and some of the rules of thumb used in this design. The goal of this report is to investigate the impact of two design choices on capsule performance: the number of "foot" pulses and the rate of change of the ion energy during the main pulse. Since the ions' range (penetration depth) depends on their kinetic energy, changing the ion energy over the course of the pulse provides an extra "knob" to optimize target gain that is unavailable to laser drivers. Laser energy is absorbed up to the critical density, which will be in the surface outer layers of the target for any laser frequency in the optical or near infrared regime.

II-2-2. Capsule model for base case: In ref. [1] a capsule was designed that consisted of a DT fuel shell, with an ablator consisting of DT wicked into a low density CH foam and with a 3 μm CH outer solid shell (used as a container) into which the DT is injected to create the DT shells. A later version of this target that had a larger ratio of shell thickness to radius, that improved stability, has been subsequently studied. The total pulse energy for this target was 0.44 MJ, that was delivered in three 50 MeV rubidium (Rb) "foot pulses" (at 1.4 TW for 8.03 ns, 6.5 TW for 2.1 ns, and 30.2 TW for 0.8 ns) and one 500 MeV Rb "main pulse" (at 205 TW flattop for 1.74 ns). This target ignited to release a fusion yield of 20.8 MJ, a gain of 47.3 over the total pulse energy. As mentioned in the introduction, a new base case target was designed based on a hydrodynamically scaled version of this latter ~0.5 MJ target. The scaling was obtained by applying a factor F to the linear dimensions of the original target. The mass of the new target and hence the total energy in the ion pulse scales as F^3, and the power on target scales as F^2, assuming a constant ion flux.

For a reactor-grade target, we chose F=2.25, corresponding to a scaled pulse energy of 5.695 MJ. However, the optimum gain was found at 3.7 MJ of heavy ion drive. Fig. 13 displays the radial trajectories of a number of fluid elements in a 1-D simulation of this base case, using a total of four shocks to compress and accelerate the shell.

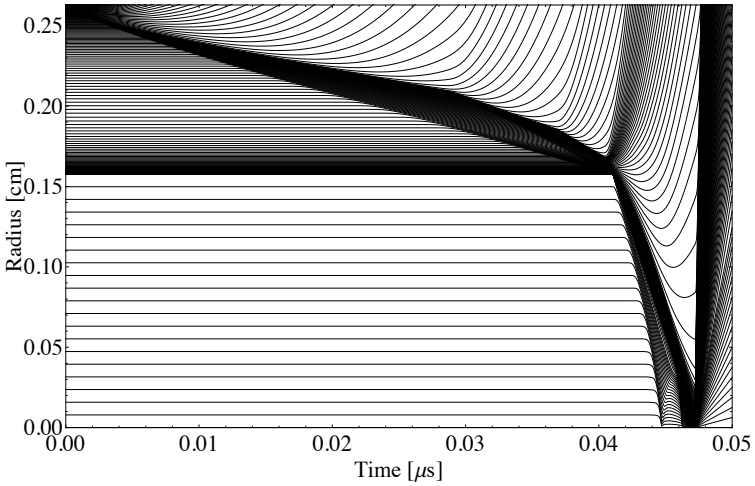

Figure 13. Lagrangian illustration of the 3.7 MJ baseline target's compression and burn. The strong shock due to the main pulse precedes the fuel shell as they travel inward, beginning at 0.04104 μs, eventually reflecting at the center of the target (0.4472 μs) and slowing the fuel shell upon collision (0.04579 μs). Ignition occurs at 0.0459 μs. The foot shocks can be seen beginning at 0.00025, 0.0286, and 0.0368 μs.

We chose a high ion mass (Mercury, Hg) to maximize stopping and therefore maximize ion energy, which allows minimal ion current. The ion energy is determined by requiring the stopping length to be at the same fraction of the capsule radius as in the 0.44 MJ target. This yielded an ion energy of 2.21 GeV for the main pulse and 220 MeV for the foot pulses.

2-II-3. Dependence of gain on number of shocks (intensity variations): The basic

strategy for designing the capsule follows the discussion in ref. [2]. A small number (typically ~3) of "foot" shocks compress the fuel at a low adiabat (α), defined here as the ratio of the fuel pressure to the electron degeneracy pressure at the given fuel density and material composition. In the high-density limit ($\rho >> 1$ g•cm^{-3}), interatomic binding becomes unimportant and the degeneracy pressure asymptotes to [3]

$$p_{\mathrm{Fermi}} = \frac{2}{5}\frac{\hbar^2}{2m_e}\frac{\left(3\pi^2\right)^{2/3}}{\left[\left(m_D + m_T\right)/2\right]^{5/3}}\rho^{5/3} \approx 2.21\left(\frac{\rho}{1\ \mathrm{g/cm^3}}\right)^{5/3}\ \mathrm{Mbar} \qquad (6)$$

where m_e, m_D, and m_T are the electron, deuteron, and triton masses, respectively. The foot shocks are followed by a short intense main pulse that further compresses and accelerates the dense shell just assembled.

The sequence of shocks approximates adiabatic compression which would allow large densities and hence large areal densities ρR, needed for efficient fusion burns. In ref. [2], chapter 4 it was shown that a large number of *laser*-driven shocks slowly increasing in pressure can approach the adiabatic result. In this section, we investigate whether the same applies to ion beams, where the deposition is more volumetric. We thus vary the number of foot pulses (N_s) from zero to four and investigate how this affects the adiabat and ultimately the fusion gain.

Each of the foot pulses creates a strong foot shock that maximally compresses the DT fuel as it propagates inwards. For a monatomic, $\gamma = 5/3$, gas, this is a factor of $(\gamma+1)/(\gamma-1)=4$ increase in density. However, the fuel pressure and entropy may increase without bound on the shock Hugoniot: the ion beam power flattops must be tailored to minimize the entropy each shock adds to the fuel. Ref. [2] advises that the pressures of any two serial shocks be constrained $P_{i+1}/P_i < 4$ to keep the fuel nearly Fermi degenerate. The foot pulse intensities were chosen to increment the pressure in the fuel by factors of $100^{1/N_s}$, beginning at 1 Mbar. For example, in the $N_s = 3$ case, the drive pressure due to the first foot shock was initially 1 Mbar. The second and third shocks increased the pressure at the fuel to 4.64 Mbar and 21.54 Mbar, respectively. The drive pressure due to the main pulse (~300 Mbar) was chosen to optimize the fusion gain of the $N_s = 3$ case. A lower pressure ratio is possible with a larger number of foot pulses, better approximating adiabatic compression.

In ICF, the figure of merit is the in-flight adiabat, evaluated at the instant of the shell's peak kinetic energy after acceleration by the main pulse. The adiabat determines the compressibility of the fuel and consequently the areal density that may be assembled. The same main pulse (4.62 ns at 683 TW) was used in each case, applied after all foot shocks had passed through the fuel. This choice keeps the maximum drive pressure constant between all five cases and isolates variations in target parameters due to the details of the compression schedule. In the $N_s = 0$ case, the main pulse was applied directly to the uncompressed, Fermi degenerate target.

Fig. 14 indicates that the in-flight fuel adiabat decreased monotonically as N_s was increased. Likewise, the assembled ρR and fusion gain increased monotonically.

Ignition (gain > 1) was demonstrated for $N_s \geq 2$, $\alpha \leq 3.16$, and $\rho R \geq 2.19$ g•cm^{-2}.

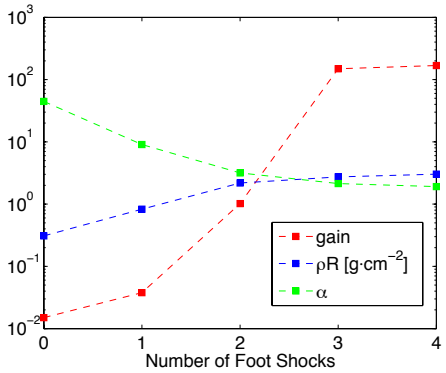

Figure 14. Variation of fusion gain, assembled areal density, and in-flight adiabat, with the number of compressive foot shocks.

A rule of thumb in ICF target design concerns the diminishing returns provided by increasing N_s: the adiabat typically asymptotes for $N_s > 3$. This behavior is evident from fig. 14: increasing the number of foot shocks from three to four reduces the adiabat by only 10%. The $N_s = 3$ adiabat of 2.13 is comparable to the current NIF CH ablator baseline target's adiabat of 1.51 [4]. Future work is needed to determine whether this difference is due to the thicker target design employed here or the volumetric energy deposition of the heavy ion beam driving the implosion. In any event, the convergence ratios (e.g. 28.9 for $N_s = 3$) achieved by these targets are close to the ceiling imposed by hydrodynamic instabilities: further reducing the adiabats may have the effect of increasing mix to unacceptable levels.

2-II-4. Dependence of gain on ion energy ramping of main shock: In ref. [1], the argon ion kinetic energy is held fixed at 50 MeV for the entire drive. When the energy deposition raises the electron thermal velocity above the directed velocity of the argon ions, their range in the target increases. This passive range lengthening allows the energy deposition to penetrate the expanding plasma corona blown off the ablating target. Due to solid angle effects, the drive is more efficient if absorption occurs at a smaller radius, closer to the ablation front. Likewise, stopping within stagnant or ingoing material can contribute proportionally more ion kinetic energy to the ingoing fuel shell. To ease ion current demands in the driver, we are considering high-energy, short-range mercury ions for an active approach to range lengthening: increasing the ion kinetic energy as ablation proceeds inward.

For the drive histories detailed in 2-II-3, most of the target mass is ablated during the 683 TW main pulse, which delivers most of the drive energy. Improving the coupling of the main pulse energy could therefore substantially increase the fusion yield, which is very sensitive to the velocity of the fuel shell [2]. In the case of a pulse of a constant ion energy (fig. 15), it is observed that the coupling is poor, with the high-energy mercury ions initially penetrating deep within the fuel before backing off as the plasma corona grows. In this case and in all runs to be discussed later, the $N_s = 3$ foot pulses at a constant ion energy of 221 MeV were used to compress the target.

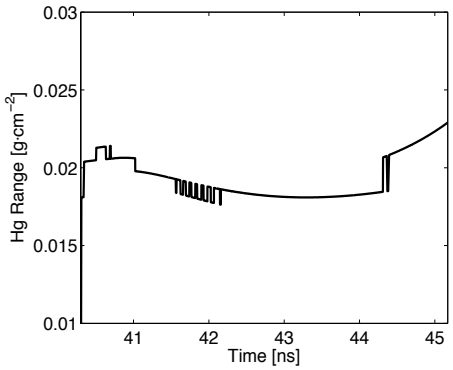

Figure 15. Range of beam ions in the 683 TW main pulse following three foot shocks (N_s = 3 case). The mercury ions' incident kinetic energy is fixed at 2.21 GeV for the duration of the 4.2 ns pulse.

This has the effect of raising the fuel adiabat–essentially heating the target–instead of accelerating the shell inward. Fig. 16 demonstrates that the subsequent range shortening reduces the amount of beam energy that penetrates the plasma corona. It is evident that a constant ion energy pulse overheats the fuel at the outset (range too high at early time) and is then inefficiently absorbed in the blow off plasma (range too low at late time).

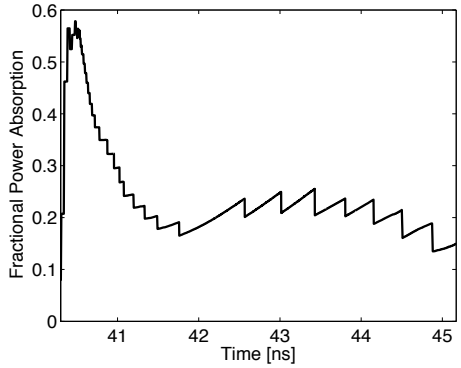

Figure 16. Fractional power absorption in ingoing material for the same constant-energy pulse as fig. 15.

Linear ramps of the beam ions' kinetic energy have been explored with the goal of providing the most efficient drive during all phases of the main pulse. Fig. 17 demonstrates that even a slight variation in ion kinetic energy over the main pulse can improve the coupling efficiency. When the initial kinetic energy is lowered from 2.21 GeV, the coupling efficiency passes through a maximum before falling due to inadequate ion range during the entire pulse.

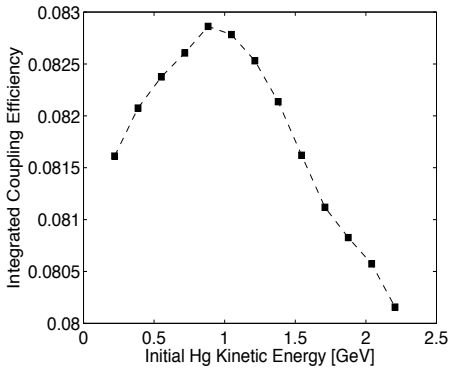

Figure 17. Integrated coupling efficiencies (ratios of shell kinetic energy to total driver energy) for main pulses with ion kinetic energies ramped to 2.21 GeV. Note that the rightmost data point is the constant, 2.21 GeV case: there is a clear benefit to lowering the incident mercury energy early in the main pulse.

Each main pulse considered was applied to the same shell assembled by three foot shocks (N_s = 3 case). Fig. 18 illustrates the beam ion range resulting from a ramp located in a broader sweep of ion kinetic energies (cf. fig. 15). Note that the duration and intensity of the main pulse are unchanged: only the beam ion energy has been adjusted. Fig. 19 shows that the ion energy ramping has addressed both liabilities of a constant-energy main pulse: there is no initial penetration to the fuel and energy is efficiently transferred to the shell even at the end of the pulse.

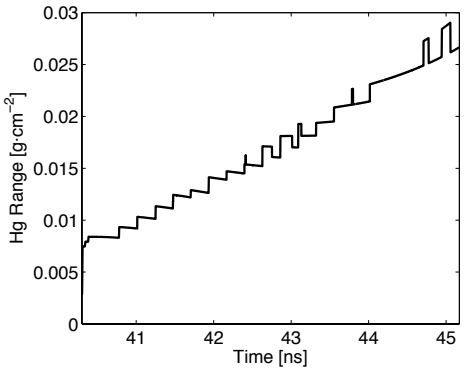

Figure 18. Range of beam ions ramped from 0.98 GeV to 3.0 GeV over the course of the main pulse.

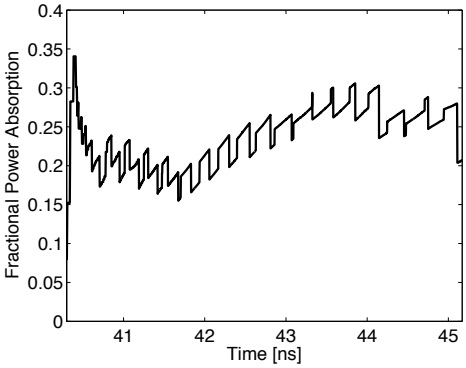

Figure 19. Fractional absorption of a ramped main pulse within ingoing material. The lack of an initial overshoot in ion range is evident, along with the nearly constant deposition efficiency at late time (cf. fig. 16).

The kinetic energy ramping in the main pulse (0.98 GeV to 3.0 GeV, cf. constant 2.21 GeV) improved the fusion gain from 149.4 to 161.8. The hydrodynamic coupling efficiency improved to 8.98% from 8.02 %; the fuel kinetic energy increased from 0.267 MJ to 0.290 MJ. The in-flight adiabat was lowered from 2.13 to 1.67: the beam added significantly less thermal energy to the fuel mass.

Evidently, there is substantial motivation for energy ramping in the main, accelerating pulse of heavy ion direct drive shots. The coupling efficiency and fusion gain may both be increased at constant integrated drive energy. However, velocity tilts of only ~10% have been demonstrated with induction lilacs at present [5-6]. The high-efficiency pulse shape presented here would require a head-to-tail tilt of almost 75%. Marginal improvements in integral parameters are possible with more modest tilts. The low ion energy early in a ramped, high-intensity main pulse may also place more strenuous current requirements on the accelerator than a constant, higher-energy pulse. More work is needed to explore other possible pulse shapes and ultimately implement self-consistent ion energy histories.

2-II-5. Conclusion

We have used HYDRA to study the effects of two important design choices on ICF target performance. We have shown that increasing the number of foot pulses may substantially reduce the target's in-flight adiabat and consequently improve its compressibility and fusion yield. As in the case of laser drive, the first three shocks are the most important to the target's performance, with additional shocks contributing only marginally to compression and burn. We have also demonstrated that ion range lengthening during the main pulse can further reduce the target adiabat and improve the efficiency with which beam energy is coupled into the target. The ideal beam energy spread is difficult to implement with current accelerator technology, but incremental improvements in fusion gain are still possible.

2-II-6. References

[1] B. G. Logan, L. J. Perkins, and J. J. Barnard, Phys. Plasmas 15, 072701 (2008).
[2] J. D. Lindl, Inertial Confinement Fusion, The Quest for Ignition and Energy Gain Using Indirect Drive, (Springer-Verlag, New York, 1998).
[3] S. Atzeni, and J. Meyer-Ter-Vehn, The Physics of Inertial Fusion: Beam Plasma Interaction, Hydrodynamics, Hot Dense Matter (Oxford University Press, 2004).
[4] D. S. Clark *et al. Phys. Plasmas* **17**, 052703 (2010).
[5] P. K. Roy *et al. Phys. Rev. Lett.* **95**, 234801 (2005)
[6] A. Friedman *et al. Nucl. Instr. And Meth. A* **606** (2009) pp 6-10.